RESEARCH ARTICLE

Mitochondrial dysfunction and cell death induced by Toona sinensis leaf extracts through MEK/ERK signaling in glioblastoma cells

Yu-Feng Su[1,2,3], Tai-Hsin Tsai[1,3], Keng-Liang Kuo[1], Chieh-Hsin Wu[1,3], Hui-Yuan Su[1], Wen-Chang Chang[4], Fu-Long Huang[5], Ann-Shung Lieu[1,3], Aij-Lie Kwan[1,3], Joon-Khim Loh[1,3], Chih-Lung Lin[1,3], Cheng Yu Tsai[1,2,3,6,7]*

1 Division of Neurosurgery, Department of Surgery, Kaohsiung Medical University Hospital, Kaohsiung, Taiwan, **2** Department of Surgery, Post Baccalaureate Medicine, College of Medicine, Kaohsiung Medical University, Kaohsiung, Taiwan, **3** Department of Surgery, School of Medicine, College of Medicine, Kaohsiung Medical University, Kaohsiung, Taiwan, **4** Department of Food Science, National Chiayi University, Chiayi, Taiwan, **5** Department of Food Nutrition, Chung Hwa University of Medical Technology, Tainan, Taiwan, **6** Division of Neurosurgery, Department of Surgery, Kaohsiung Medical University Gangshan Hospital, Kaohsiung, Taiwan, **7** Graduate Institute of Medicine, College of Medicine, Kaohsiung Medical University, Kaohsiung, Taiwan

* moutzyy691010@yahoo.com.tw

OPEN ACCESS

Citation: Su Y-F, Tsai T-H, Kuo K-L, Wu C-H, Su H-Y, Chang W-C, et al. (2025) Mitochondrial Dysfunction and Cell Death Induced by Toona Sinensis Leaf Extracts through MEK/ERK Signaling in Glioblastoma Cells. PLoS One 20(5): e0320849. https://doi.org/10.1371/journal.pone.0320849

Editor: Javier S Castresana, University of Navarra, SPAIN

Received: October 31, 2023

Accepted: February 26, 2025

Published: May 9, 2025

Peer Review History: PLOS recognizes the benefits of transparency in the peer review process; therefore, we enable the publication of all of the content of peer review and author responses alongside final, published articles. The editorial history of this article is available here: https://doi.org/10.1371/journal.pone.0320849

Abstract

Toona sinensis, a kind of phytochemicals in traditional Chinese medicine widely used in South-East Asia, has been recognized for its anticancer properties, particularly against various types of cancer. We aimed to evaluate the effectiveness of T. sinensis leaf extracts (TSL) specifically for glioblastoma multiforme (GBM). Gallic acid was identified as the major active component in the aqueous extracts of TSL using the HPLC system. Furthermore, it has been shown to have the ability to penetrate the blood-brain barrier. Various concentrations of TSL (10, 20, 40, and 80 μg/mL) were applied and 80 μg/mL TSL treatment significantly inhibited cell growth, proliferation, and cytotoxicity in A172 and U251 GBM cells. Flow cytometry analysis revealed cell cycle arrest at the G2/M phase and increased apoptotic cells. Furthermore, we observed mitochondrial dysfunction characterized by elevated ROS levels and reduced ATP production due to the blockade of electron transport chain (ETC) complexes. TSL treatment regulated this ROS-induced mitochondrial dysfunction. Western blotting analysis showed upregulation of Bax and Puma, along with downregulation of Bcl-2. Additionally, TSL treatment induced the cleavage of caspase-3, caspase-9, and PARP, indicating activation of the mitochondria-mediated apoptosis pathway and caspase-dependent pathway in both GBM cell lines. To investigate the involvement of the MEK/ERK pathway in TSL-induced effects, we used U0126, an inhibitor of MEK/ERK kinase. The results demonstrated that TSL treatment suppressed MEK/ERK activation, inhibiting ROS-induced mitochondrial dysfunction and promoting apoptosis. This suggests a potential therapeutic strategy targeting the MEK/ERK pathway in GBM treatment. Overall, our findings indicate that TSL

Data availability statement: All relevant data are within the manuscript and its Supporting Information files.

Funding: This work was supported by Kaohsiung Medical University Chung-Ho Memorial Hospital KMUH110-0M27, KMUH111-1T02 (awarded to Cheng Yu Tsai) and KMUH105-5T05 (awarded to Yu-Feng Su); and Kaohsiung Municipal Ta-Tung Hospital KMTTH-107-028, KMTTH-108-011, KMTTH-109-037 (awarded to Yu-Feng Su).

Competing interests: The authors have declared that no competing interests exist

treatment exerts cytotoxic effects through ROS-mediated mitochondrial dysfunction and activation of apoptotic pathways via MEK/ERK pathway in GBM cells. These insights provide valuable knowledge for potential therapeutic applications of TSL in GBM treatment.

Introduction

Glioblastoma multiforme (GBM) is one of the most devastating tumors, with poor prognosis and high recurrence rates. It was recognized as grade IV astrocytoma according to the World Health Organization [1] and accounts for 40% of all primary brain tumors and 78% of malignant central nervous system tumors [2]. Even after standard surgical excision and concomitant radiation and chemotherapy (CCRT), the mean survival time remains <15 months [3,4]. The poor prognosis of GBM is related to glioma cells' natural invasive characteristics and therapeutic resistance, including chemoresistance and radioresistance [5]. The current standard chemotherapy for GBM is temozolomide, an oral alkylating agent that in-duces G2/M arrest, leading to apoptosis [6,7]. However, the overexpression of O6-53 methylguanine methyl-transferase (MGMT) in GBM cells can reverse the methylation of the O6 position of guanine, causing DNA damage repair and chemoresistance [8,9]. In developing evidences revealed that MEK/ERK pathway is considered to enhance survival and confer resistance against radio- and chemotherapy [10]. In GBM treatment, the MEK/ERK pathway enhances cell migration and invasion in response to treatment, and increases DNA damage repair both through non-homologous end joining repair as well as homologous recombinational repair pathways [11]. Therefore, developing new strategy agents in EMK/ERK pathway for GBM treatment is paramount. Therefore, developing new strategy agents in MEK/ERK pathway for GBM is paramount.

Chemotherapy and radiation therapy share common pathways to cell death, inducing direct or indirect DNA damage through the generation of ROS [12]. Although low levels of mitochondrial ROS enhance cell growth, higher levels induce apoptosis [13,14]. Thus, in many cancers, the ROS production level is an import-ant marker of the state of the tumor and in-creasing ROS generation is considered an anticancer effect. High ROS levels induce cyto-toxicity and reverse chemo-therapeutic resistance in tumorigenic cells, and ROS production causes therapy resistance [15,16]. In essence, ROS production is induced by mitochondrial dys-function or mitochondrial dysfunction from redox aberrations (e.g., hypoxia, cellular degradation, or detoxification processes) and may synergistically promote cancer progression, even in the presence of drug resistance [17]. Thus, regulation of ROS-regulated mitochondrial dysfunction is a promising anticancer factor.

Toona sinensis (A. Juss) M.J. Roem., is a type of edible vegetable that is widely applied in South-East Asia as a type of traditional Chinese medicine (TCM) in clin-ical practice [18]. The most abundant ingredients in T. sinensis leaf (TSL) extracts include gallic acid (10%), rutin (0.5%), quercetin (0.42%), quercitrin (0.15%), kae-mpferol 3-O-b-D-glucoside (0.06%), methyl gallate (0.02%), ethyl gallate (0.002%),

quercetin 3-O-b-D-glucoside (<0.002%), and kaempferol (<0.002%) [19]. TSL aqueous extracts have various biopharmacological activities, including antioxidant [20,21], anti-diabetes [22], neuron degenerative disease–suppressing [23], anti-inflammation [24], antivirus [25], and anticancer [26,27] properties. TSL treatment inhibits cancer cell growth in lung cancer [28], prostate cancer [27], and acute myeloid leukemia [29]. JAK2/stat3, Akt, MEK/ERK, and mTOR/HIF-2α pathways have also been reported as potential pathways for inhibition of renal carcinoma cell growth and migration under TSL treatment [30]. Moreover, gallic acid was viewed as the most major component in TSL and was reported in anti-cancer effect via reactive oxygen species (ROS)-mediated pathway in prostate cancer. However, the underlying molecular mechanisms remain unclear.

In this study, we confirmed that gallic acid was the major effective components in aqueous extracts in TSL and it could penetrate across blood-brain barrier (BBB). Then we explored if and how TSL treatment affects GBM. We demonstrated that TSL treatment induced apoptosis and cell cycle arrest to exert cytotoxic effects in two glioblastoma cell lines. ROS-regulated mitochondrial dysfunction was detected and the exhibition of ROS increased, followed by a decrease in mitochondrial transmembrane potential (ΔΨm) and ATP production under TSL treatment. Intrinsic mitochondria-mediated apoptosis and the caspase-dependent pathway were also detected by an increase in BAX/Puma and decrease in Bcl-2, accompanied by increased cleaved caspase-3, cleaved caspase-9, and cleaved caspase-PARP. The MAPK/ERK signaling pathway was responsible for the potential pathway through the use of U0126. Finally, our findings revealed that TSL treatment can induce apoptosis through ROS-regulated mitochondrial dysfunction via the MEK/ERK signaling pathway and antiox-idant effect in human glioblastoma cells.

Materials and methods

Materials

The TMRM Reagent and CellROX™ Green Reagent were procured from Invitrogen (Life Technologies, CA, USA). Other reagents, including bovine serum albumin (BSA), RNase A, propidium iodide (PI), carbobenzoxy-valyl-alanyl-aspartyl-[O-methyl]-fluoromethylketone (Z-VAD-FMK), dihydroethidium (DHE), and the ATP Assay Kit, were obtained from Sigma-Aldrich (St. Louis, MO, USA). The MEK Inhibitor U0126 was sourced from Promega (Madison, WI, USA), while the specific ERK activator IKVAV (Isoleucyl-lysyl-valyl-alanyl-valine), ERK activator tBHQ (tert-Butylhydroquinone), antioxidant N-acetylcysteine (NAC), and Cell Counting Kit-8 (CCK-8) were purchased from TargetMol (Boston, MA, USA). The Annexin V-FITC/PI apoptosis detection kit came from Fremont (CA, USA). The GAPDH antibody was acquired from Santa Cruz Biotechnology (Santa Cruz, CA, USA), and antibodies specific for phospho-ERK1/2 (T202/Y204), ERK1/2, puma, Bax, Bcl-xL, Caspase-3, Caspase-9, and PARP were procured from Cell Signaling Technology (Beverly, MA, USA). The total oxidative phosphorylation (OXPHOS) rodent WB antibody cocktail (Mouse) was obtained from Abcam (Cambridge, MA, USA). Secondary horseradish peroxidase (HRP) conjugated donkey anti-rabbit and donkey anti-mouse antibodies were sourced from Invitrogen (Life Technologies, CA, USA).

HPLC System

An HPLC equipped with a pump (Hitachi Model L-2130 delivery pump, Tokyo, Japan), diode array detector (Hitachi L-7455 absorbance detector, Tokyo, Japan), and an injector was used. A RP-18 column (Kanto Chemical Co. Inc., Tokyo, Japan) was used for the HPLC system. Standard phenolic acid solutions were filtered through a 0.22 μm pore membrane filter before injection and crude extract was centrifuged and then filtered through a 0.22 μm pore membrane filter before injection. The injection volume for all samples was 20 μL. The mobile phase consisted of 2 solvents: Solvent A, acetic acid (2%) and Solvent B, acetonitrile/acetic acid (0.5%) (1:1; v/v). The mobile phase was filtered through a 0.22 μm pore membrane filter and degasified with ultrasound. Phenolic compounds were eluted under the following conditions: 1 mL/min flow rate and the column temperature was set at 25°C, isocratic conditions linear gradient conditions from 0% to 10% B in 10 mins, from 10% to 40% B in 40 mins, from 40% to 55% B in 15 mins, from 55% to 80% B in 5 mins, from 80 to 100% B

in 5 mins, followed by washing and reconditioning the column. For detection, chromatograms were monitored by diode array detector, which were recorded for all peaks. Duplicate analyses were performed for each sample. The identification of phenolic compounds was obtained by using authentic standards.

Preparation of Aqueous Extracts of Toona Sinensis Leaf (TSL)

The TS leaves used in this preparation were obtained from TS grown in Tuku (Yunlin County, Taiwan) and were picked and washed thoroughly with water. A voucher specimen (FY-001) was characterized by Dr. Horng-Liang Lay, Graduate Institute of Biotechnology, National Pingtung University of Science and Technology, Pingtung County, Taiwan, and deposited at Fooyin University, Kaohsiung. Permissions were also obtained by Dr. Horng-Liang Lay. In brief, the liquid of TSL was concentrated in a vacuum and freeze-dried to form a powder. The TSL aqueous extracts used in experiments were dissolved in sterile phosphate-buffered saline (PBS; pH 7.4) and filtered using a 0.45-mm syringe filter (Satorius Stedim Biotech Inc., Goettingen, Germany) [31].

Model to predict BBB permeation

The ability of compounds (Gallic acid) to cross the BBB by passive diffusion was predicted by BBB predictor (https://www.cbligand.org/BBB/). This online predictor offered corresponding calculation of the BBB score, which indicates whether a compound can cross (BBB^+) or not (BBB^-). The threshold of the BBB^-/BBB^+ score is 0.02.

Cell culture

Human GBM cell lines (A172 [ATCC CRL-1620; ATCC] and U251 [ormerly known as U-373 MG; ECACC 09063001]) were obtained from American Type Culture Collection, (ATCC, Manassas, VA, USA). The culture of A172 and U251 cells was performed in Dulbecco's Modified Eagle Medium (DMEM) containing 10% fetal bovine serum (FBS) and 1% penicillin–streptomycin (100 units/ml of penicillin and 10 mg/ml of streptomycin; all from Gibco; Thermo Fisher Scientific, Waltham, MA, USA) and incubated in a 5% CO2 incubator at 37 °C with fully humidified conditions. All experiments were performed when cells were in the logarithmic phase of growth.

Cell viability and colony formation assay

A CCK-8 assay was employed to assess cell viability. In brief, GBM cells (A172: 2×10^4 cells/well and U251: 2×10^4 cells/well) were seeded in 96-well plates overnight. Subsequently, the cells were treated with varying concentrations of TSL (10, 20, 40, 80, and 160 μg/mL) at 37°C for 24, 48, and 72 hours. Following the incubation period, 1/10 volume of Cell Counting Kit-8 (CCK-8) was added directly to the cells in the culture medium. The mixture was then incubated in a cell culture incubator for 1–4 hours at 37°C until the color turned orange. Absorbance at 450 nm was measured using a Synergy™ HT Multi-Detection Reader (Bio-Tek Instruments, Winooski, VT). Additionally, colony formation assays were conducted following established procedures [32]. GBM cells were seeded in triplicate in 6-well plates at a density of 1000 cells/well. After an overnight culture, the cells underwent pretreatment with various concentrations of TSL (0, 10, 20, 40, 80, and 160 μg/mL). Subsequently, the cells were incubated at 37 °C for an additional 14 days to facilitate colony formation, and the resulting colonies were stained with crystal violet. Finally, the purple formazan crystals were dissolved in 1 ml of DMSO, and the absorbance was measured at a wavelength of 570 nm.

Cell cycle analysis

For cell cycle analysis, cultured A172 and U251 cells, following treatment with increasing concentrations of TSL for 48 h, were collected and washed with PBS (pH 7.2). The cells were resuspended in 85% methanol for overnight at 4°C and then centrifuged at 1500rpm for 10 min. The resultant pellet was washed twice with PBS, suspended in PBS and incubated with stained

with 100 μg/mL propidium iodide (PI, Sigma-Aldrich Co) and RNase (20 Units/mL, final concentration) for 30 min. At least 10,000 cells were counted by a flow cytometer (Attune NxT flow cytometer, Thermo Fisher Scientific), and the data obtained were analyzed using and the data obtained were analyzed using Attune NxT Flow Cytometer Software (Thermo Fisher Scientific).

Apoptosis analysis

A172 and U251 cells were treated with various concentrations of TSL in the presence or absence of z-VAD (10 μM), U0126 (10 μM), tBHQ (50 μM) or IKVAV (0.5 mM) for 48 hours. Apoptosis was assessed using the CF®488A Annexin V and PI Apoptosis kit. Phosphatidylserines exposed on the membrane surface of apoptotic cells were stained with Annexin V-FITC according to the manufacturer's instructions. Late apoptotic (or necrotic) cells were stained with PI. Additionally, A172 and U251 cells were pretreated with 10 mM NAC for 30 min before being treated with 80 μM TSL for 48 hours. Apoptosis was then measured using a flow cytometer.

Determination of the intracellular ROS, mitochondrial ROS and ΔΨm

Intracellular ROS production was detected using CellROX, mitochondrial ROS production was detected using DHE and ΔΨm production was detected using TMRM. Following incubation A172 and U251 cells with the different doses of TSL for 48 h, 5 μM CellROX® green reagent, 250 nM DHE red reagent and 25 nM TMRM at 37 °C for 30 min. Subsequently, the cells were washed in PBS, trypsinized and measured fluorescence intensity by flow cytometry at excitation/emission wavelengths of 485/530 nm, 510/580 nm and 488/570 nm for CellROX, DHE and TMRM, respectively, and the results were analyzed using Attune NxT Flow Cytometer Software.

Cell ATP levels

Cultured A172 and U251 cells, following treatment with increasing concentrations of TSL for 48 h, were collected and washed with PBS (pH 7.2). Cell ATP measurement were conducted as described previously [33]. Then sample was measured with absorbance at 570 nm (A570) or the fluorescence (FLU, lex = 535/ lem = 587 nm) in a microplate reader. For each measurement, a standard curve will be constructed using serial dilutions of ATP stock solution.

Western blot analysis

Cells were seeded into 10 cm dish plates, treated different concentrations of TSL in the presence or absence of z-VAD (10 μM) or U0126 (10 μM) for 48 h. Cell lysis, protein concentration, SDS-PAGE gel and western blotting were performed as described previously [34]. The following antibodies dilutions were used for immunodetection: PARP (1:1,000, Cell signaling, Beverly, MA, USA); caspase-3 (1:1,000, Cell signaling, Beverly, MA, USA); caspase-9 (1:1,000, Cell signaling, Beverly, MA, USA); Bcl-2 (1:1,000, Cell signaling, Beverly, MA, USA); Bax (1:1,000, Cell signaling, Beverly, MA, USA); puma (1:1,000, Cell signaling, Beverly, MA, USA); ERK1/2 (1:1,000, Cell signaling, Beverly, MA, USA); phospho-ERK1/2 (T202/Y204,1:1,000, Cell signaling, Beverly, MA, USA); GAPDH (1:5,000, Santa Cruz biotechnology, Heidelberg, Germany).

Xenograft mice in vivo assay

Six-week-old male NOD/SCID immunodeficient mice, obtained from BioLASCO Taiwan Co., Ltd, were bred and maintained in accordance with institutional guidelines for the care and use of laboratory animals. The in vivo assay was conducted under the commission of Tri-Neo Biotechnology Co., Ltd., to ensure compliance with ethical standards and technical accuracy. A total of 6×10^6 cells were implanted subcutaneously into the dorsal region of each mouse. Twelve mice were randomly divided into two groups: a control group treated with DMSO, and a treatment group receiving TSL. Starting one-week post-inoculation, tumor-bearing mice were administered either DMSO or TSL (80 mg/kg) via intraperitoneal injection three times per week for a total of ten weeks. Mice were sacrificed at the end of the tenth week. Body weight was recorded weekly prior to drug administration, and tumor weights were measured post-sacrifice.

Statistical analysis

Data were analyzed using GraphPad Prism 8 software (GraphPad Software, Inc., San Diego, CA, USA). The results are presented as the mean ± standard deviation (SD). Comparisons between groups were made using an unpaired Student's t-test, and significance levels were indicated as follows: *$p < 0.05$, **$p < 0.01$, and ***$p < 0.001$.

All statistical analyses were performed in R (v4.4.1) using the lme4, lmerTest, and emmeans packages. Tumor volume differences between treatment groups over time were analyzed using a linear mixed-effects model (LME), which included Treatment, Time, and their interaction as fixed effects, with MouseID as a random effect to account for individual variability. Model significance was assessed using ANOVA (Type III Wald F-test), and post-hoc pairwise comparisons between treatment groups at each time point were conducted using estimated marginal means (emmeans) with multiple comparison adjustments. To assess whether extreme values influenced the results, outlier detection was performed using Studentized residuals (threshold: ± 2 SD). Five data points were flagged as potential outliers; however, re-analysis after their removal showed that the treatment effect remained statistically significant ($p < 0.01$). Therefore, the full dataset was used for the primary analysis, with outlier-excluded results provided in the Supplementary Materials for transparency. All statistical tests were two-tailed, and significance was set at $p < 0.05$.

Results

Characterization of Phenolics in TSL and Prediction of BBB Permeation

HPLC system qualitatively analyzed the aqueous extracts of TSL, and the total ion map of the mass spectra in the negative ion mode is shown in Fig 1. The Fig 1A revealed the result of major chemical components from the aqueous extracts by separation on a C18 column under HPLC system. The Fig 1B was shown the 5 standard phenolic components, (1) gallic acid, (2) 5-Hydroxymethylfurfural, (3) Chlorogenic acid, (4) Vanillic acid, (5) Caffeic acid. Gallic acid was identified the major single component in aqueous extracts of TSL after analyzing the retention time, fragmentation pattern and characteristic UV spectra with conjunction with the standard phenolic components results and the literature reports in Fig 1C. We also shown the chemical structure of major component (gallic acid) in TSL. Moreover, SVM-MACCSFP BBB predictor system was used to show whether gallic acid could penetrate across the BBB. The result confirmed that gallic acid could penetrate across the BBB with score is 0.02 (Fig 1D). Therefore, the result demonstrated that gallic acid is the major effective component of the TSL aqueous extracts for further experiments and it could penetrate across the BBB.

TSL treatment induced cytotoxic effects that decreased the growth and proliferation of GBM cells

To assess the cytotoxic impact of T. sinensis on glioblastoma cells, A172 and U251 cell lines underwent treatment with TSL aqueous extract. A CCK-8 assay was utilized to evaluate cell proliferation and viability, employing varying concentrations of TSL (10, 20, 40, 80, and 160 μg/mL) at 24, 48, and 72 hours. The results revealed a dose-dependent and time-dependent increase in the cytotoxic effect of TSL, with the most significant impact observed at 48 hours. The half-maximal inhibitory concentration (IC_{50}) values of TSL in A172 cells at 24, 48, and 72 hours were 123.82 ± 21.72, 85.7 ± 8.34, and 75.24 ± 2.38 μg/mL, respectively. In U251 cells, the corresponding IC_{50} values were >160, 73.67 ± 5.21, and 54.34 ± 3.11 μg/mL, respectively (Fig 2A). Furthermore, the colony formation assay revealed that cell proliferation decreased in A172 and U251 cell lines in a dose-dependent suppression by TSL, especially in A172 (Fig 2B). Morphological examination of treated glioblastoma cells after 48 hours, with concentrations ranging from 10 to 160 μg/mL, indicated dose-dependent cell shrinkage and the presence of apoptotic vacuoles. These manifested as clusters of dying cells (CDC) in both glioblastoma cell lines, as observed in phase-contrast micrographs (Fig 2C). In summary, these findings emphasize that TSL aqueous extracts significantly diminish the growth and proliferation of GBM cells, exerting a notable cytotoxic effect. All subsequent experiments will be conducted at a unified 48 hour time point, with fixed doses of 10, 20, 40, and 80 μg/mL.

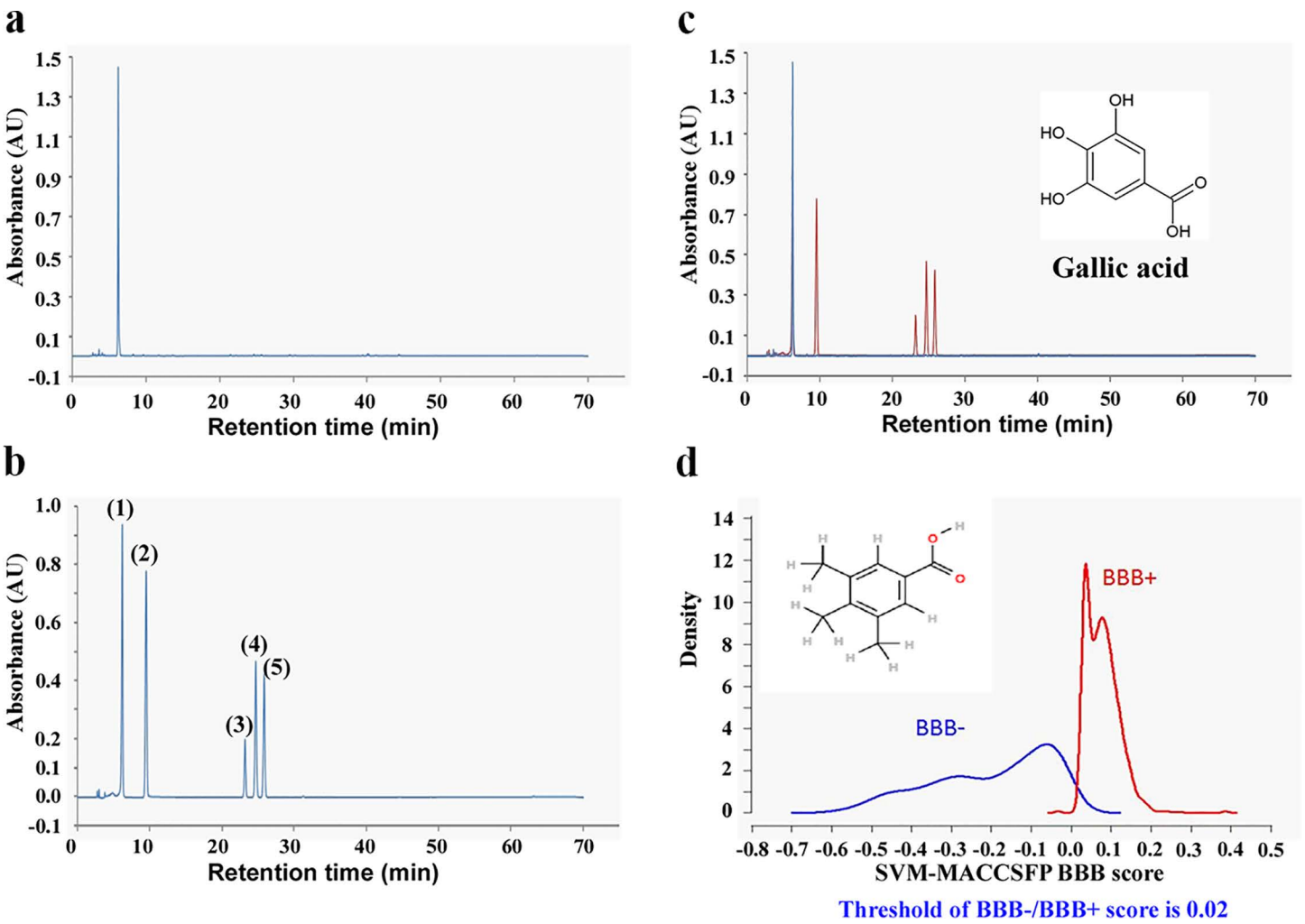

Fig 1. Characterization of phenolics of TSL. (A) major chemical components from the aqueous extracts of TSL under HPLC system analysis (B) the 5 standard phenolic components, (1) gallic acid, (2) 5-Hydroxymethylfurfural, (3) Chlorogenic acid, (4) Vanillic acid, (5) Caffeic acid. (C) Gallic acid was identified the major single component in aqueous extracts of TSL and chemical structure was shown. (D) SVM-MACCSFP BBB predictor system with BBB with score is 0.02.

https://doi.org/10.1371/journal.pone.0320849.g001

TSL treatment induced cell cycle arrest and apoptosis in GBM cells

Cell cycle arrest and apoptosis are the major cytotoxic effects of cancer treatment. We investigated whether TSL treatment (10, 20, 40, and 80 μg/mL) induced cell cycle arrest and apoptosis in the A172 and U251 cell lines. The results indicated that, under the treatment of 80 μg/mL TSL, G2/M arrest was dose-dependently induced in both cell lines, reaching 29.87% in A172 and 31.27% in U251. It is crucial to note that the S phase also exhibited a concentration-dependent increase (Fig 3A). Moreover, flow cytometry revealed that TSL treatment yielded a high percentage of apoptosis cells in the A172 and U251 cell lines (Fig 3B). Through detailed characterization of the effect of TSL treatment on cell cycle progression, we observed that TSL treatment induced a time-dependent accumulation of G2/M phase cells in the GBM cell lines. The results revealed that TSL treatment can induce cell cycle arrest, thereby suppressing cell proliferation and promoting apoptosis in GBM cells.

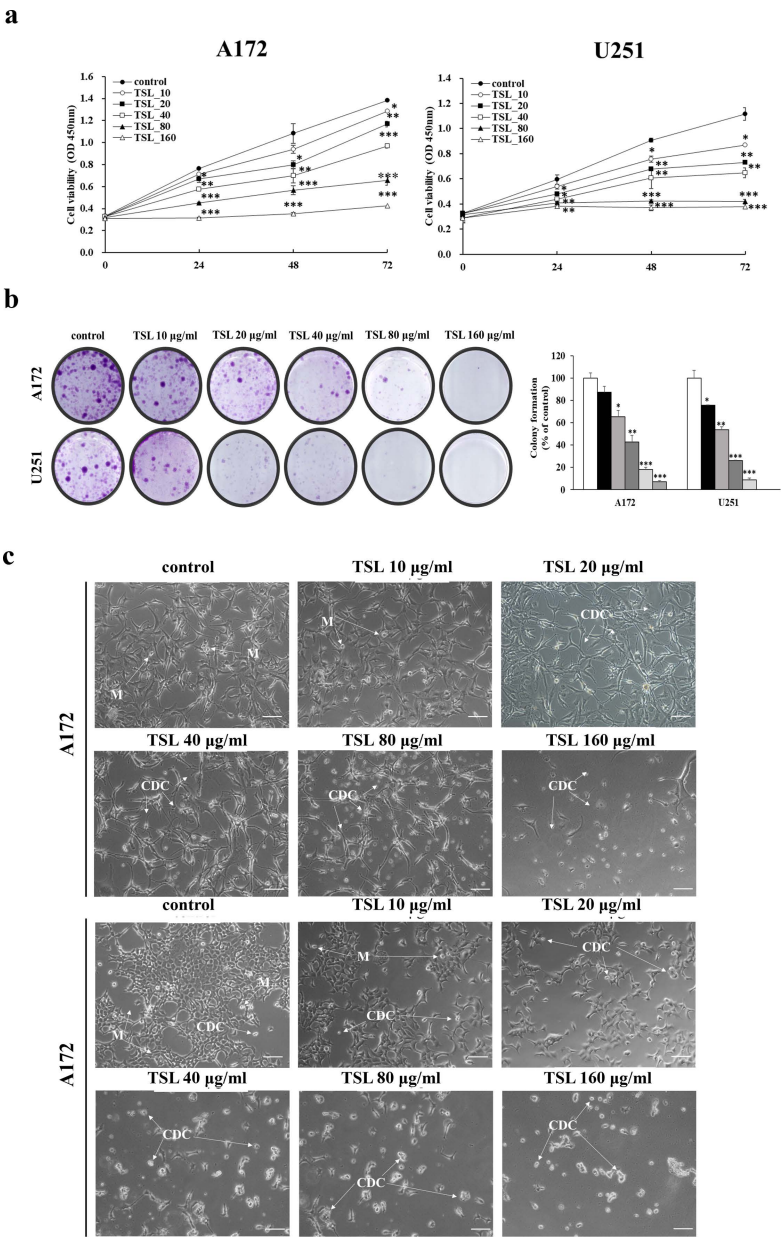

Fig 2. Effects of TSL on the viability and morphology of A172 and U251. (A) The cells (2×10^4 cells/well) were incubated with different concentrations of TSL for 24 to 72 h as described in Materials and Methods. Cell viability was measured by CCK-8 test. (B) The long-term anti-proliferative effects were evaluated in a colony formation assay. A172 and U251 GBMs cell were incubated with different concentrations of (0, 10, 20, 40, 80 and 160 μg/ml) for 16 days and assayed for colony formation. The lower panel shows quantitative analyses of colony formation. (C) Morphological illustrations of the anticancer effects observed after 48 h of culturing A172 and U251 GBMs cell with different concentrations of TSL by light microscopy (magnification ×100). The cells that are dying and detaching from the culture substrate appear white and refringent: they are labeled as CDC. The round and refringent cells are undergoing mitosis (M). All results are shown as mean ± s.d. from three independent experiments; ***$p < 0.001$, **$p < 0.01$, *$p < 0.05$ compared with the indicated control; scale bar = 100 μm.

https://doi.org/10.1371/journal.pone.0320849.g002

TSL treatment caused ROS-related mitochondrial dysfunction in GBM cells

Mitochondrial dysfunction is essential for cellular energy metabolism and cell apoptosis. Excessive ROS and decreased mitochondrial oxidative phosphorylation complexes (OX-PHOS complexes) caused a reduction in the ΔΨm and ATP

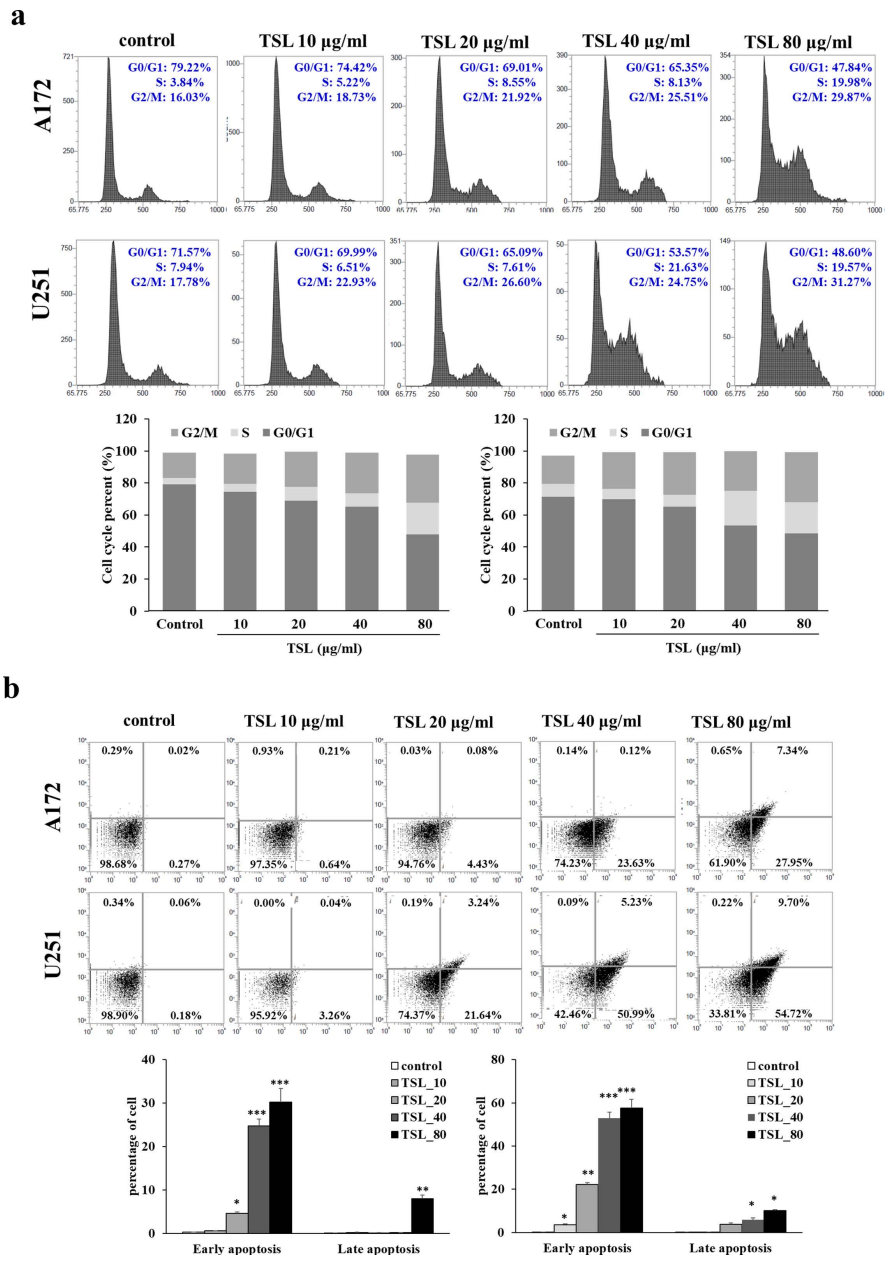

Fig 3. TSL induces apoptosis as well as cell cycle arrest in A172 and U251 GBM cells. (A) A172 and U251 cells were treated with different concentrations of TSL for 48 h, and then examined by flow cytometry to analyze the cell cycle. The proportion of cells in each cell cycle stage is shown in the graph. (B) The proportion of apoptotic cells was detected using Annexin V-FITC and propidium iodide staining. The lower panel shows percentages of cells in the early apoptosis (Annexin V^+/PI^-) together with late apoptosis (Annexin V^+/PI^+) quarters were calculated as Annexin V positive cells for statistical analysis. All results are shown as mean ± s.d. from three independent experiments; ***$p < 0.001$, **$p < 0.01$, *$p < 0.05$ compared with the indicated control.

https://doi.org/10.1371/journal.pone.0320849.g003

production, which led to mitochondrial dysfunction. To further examine whether TSL treatment induced ROS production in glioblastoma cells, we used Western blotting analysis to examine mitochondrial OXPHOS complexes, because they directly affect mitochondrial function. The results revealed significantly reduced levels of complex I, II, and IV proteins

(Fig 4A). The normalized ATP measurements, mitochondrial ROS, cytosolic ROS, and ΔΨm levels were measured using flow cytometry and fluorescence microscopy with DHE deep red, CellROX deep green, and TMRM deep red staining and presented as the mean fluorescent intensity (MFI) or percentage of the cells. The results revealed that ATP levels were significantly decreased under TSL treatment in a dose-dependent manner in the A172 and U251 cell lines (Fig 4B). In addition, mitochondrial and cytosolic ROS levels were increased under TSL treatment in a dose-dependent manner (Figs 4C and D). Eventually, ΔΨm levels were attenuated under TSL treatment in both the cell lines (Fig 4E). Collectively, the results confirmed that TSL treatment dose-dependently induced ROS-related mitochondrial dysfunction, which is affected by mitochondrial complexes I, II, and IV, in GBM cells.

TSL treatment induced apoptosis by intrinsic mitochondria-mediated apoptosis and caspase-dependent pathways in GBM cells

Multiple death signals influence mitochondrial dysfunction during apoptosis. The expression of proapoptotic factors such as BCL-2-associated X protein (Bax) and Puma, along with the antiapoptotic factor Bcl-2, play critical roles in intrinsic mitochondria-mediated apoptosis. Apoptosis is an organized, energy-dependent process of cellular self-destruction, primarily executed by proteolytic enzymes in the caspase-dependent pathway. To investigate the involvement of these proteins, we examined the expression of proapoptotic proteins (Bax and Puma) and the antiapoptotic protein (Bcl-2). Our results revealed that TSL treatment increased the levels of proapoptotic proteins Bax and Puma, while it decreased the levels of antiapoptotic Bcl-2 in both GBM cell lines (A172 and U251) (Fig 5A). Furthermore, TSL treatment elevated the levels of cleaved caspase-3, cleaved caspase-9, and cleaved PARP (Fig 5B). To confirm apoptosis via the caspase-dependent pathway, we treated the glioblastoma cells with z-VAD-FMK following TSL treatment. Flow cytometry and Western blot analyses revealed a decreased percentage of apoptotic cells and reduced levels of cleaved caspase-3, cleaved caspase-9, and cleaved PARP (Figs 5C and D). These findings demonstrate that TSL treatment induces apoptosis through intrinsic mitochondria-mediated and caspase-dependent pathways in GBM cells. As shown in Fig 4D, the levels of ROS significantly increased following TSL treatment. However, pretreatment with NAC significantly inhibited TSL-induced apoptosis in A172 and U251 cells (Fig 5E). Additionally, apoptosis-associated proteins were analyzed to validate the role of ROS in TSL-induced apoptosis. Pretreatment with NAC restored the expression levels of Bax and Bcl-2, while decreasing the levels of cleaved PARP and cleaved caspase-3 (Fig 5F). These results suggest that ROS generation is involved in TSL-induced apoptosis in GBM cells.

TSL treatment induced apoptosis through ROS-regulated mitochondrial dysfunction by inhibiting MEK/ERK signaling pathway in GBM cells

Accumulating evidence suggests that the MEK/ERK pathway plays an anti-apoptotic role by preventing mitochondrial dysfunction. Based on this, we hypothesized that TSL treatment induces apoptosis by promoting mitochondrial dysfunction through the inhibition of the MEK/ERK signaling pathway. To test this, we first examined the expression levels of ERK and phosphorylated ERK (p-ERK) in glioblastoma cells treated with TSL. Our results showed a dose-dependent reduction in p-ERK levels following TSL treatment (Fig 6A). Next, we used U0126, a highly selective inhibitor of both MEK1 and MEK2, to further confirm the role of the MEK/ERK pathway. Flow cytometry analysis indicated a more pronounced increase in apoptotic cells in the TSL and U0126 co-treatment groups compared to TSL treatment alone, across both glioblastoma cell lines (Fig 6B). Furthermore, we observed elevated levels of cleaved caspase-3, cleaved caspase-9, cleaved PARP, and pro-apoptotic protein Bax, while ERK/p-ERK and anti-apoptotic protein Bcl-2 levels significantly decreased in the co-treatment groups (Figs 6C and D). To further investigate the involvement of the ERK signaling pathway in TSL-induced apoptosis, we treated A172 and U251 cells with tBHQ (an ERK activator) or IKVAV (a specific ERK activator) and evaluated cell viability after TSL treatment. The presence of tBHQ and IKVAV effectively suppressed TSL-induced apoptosis (Figs 6E and G).

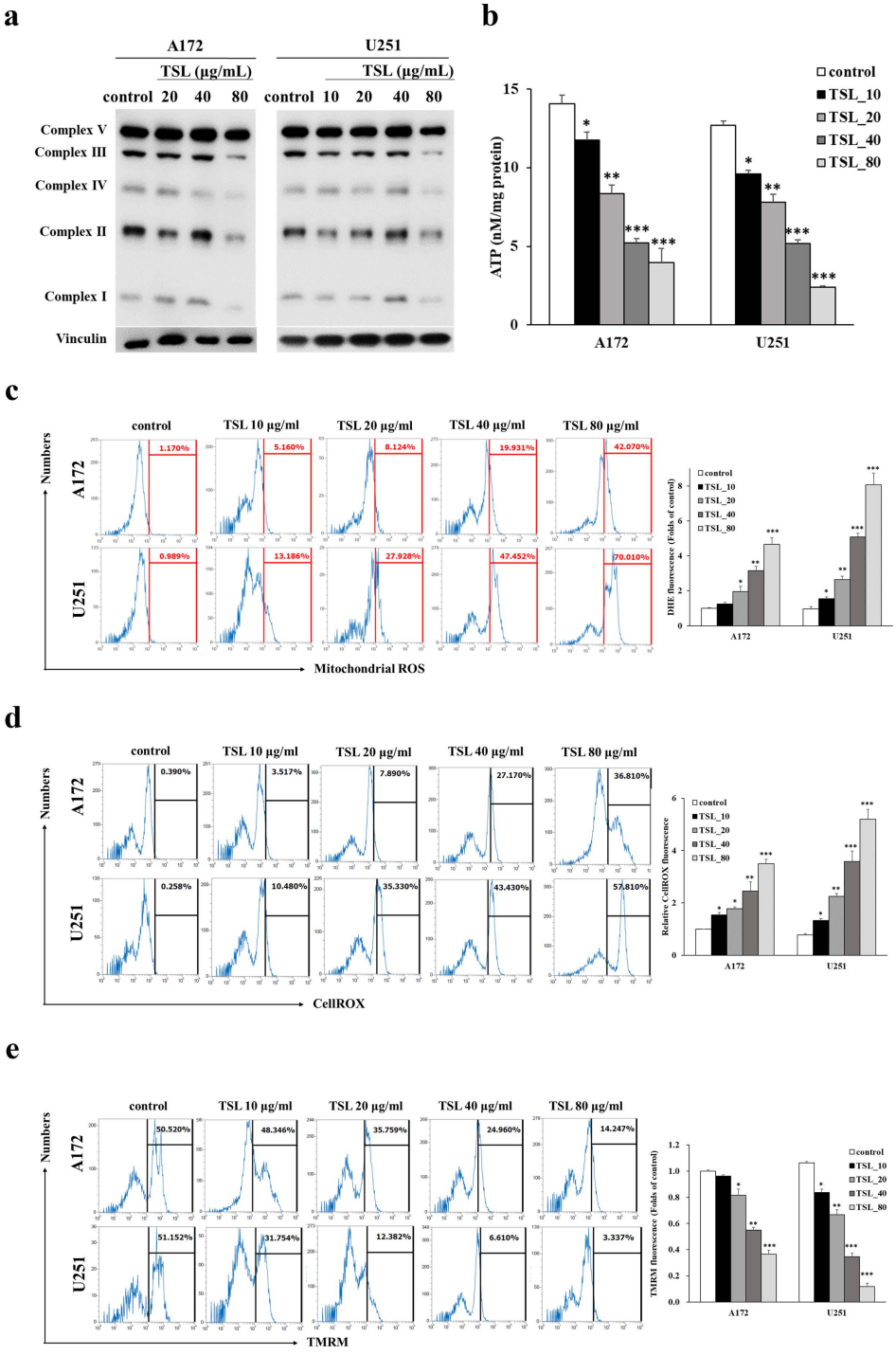

Fig 4. Increases in mitochondrial ROS associated with ΔΨm decreases in TSL-treated cells. (A) Effect of TSL on the expression of OXPHOS-related protein complexes in A172 and U251. (B) Normalized ATP measurements in A172 and U251 cells. (C) mitochondria ROS, (D) cytosolic ROS and (E) ΔΨm levels were measured using flow cytometry and fluorescence microscopy with DHE deep red, CellROX Deep green, and TMRM deep red staining, respectively, and indicated by representative histograms are shown in parallel with bar graphs showing the relative TMRM mean relative fluorescence intensity. All results are shown as mean ± s.d. from three independent experiments; ***$p < 0.001$, **$p < 0.01$, *$p < 0.05$ compared with the indicated control.

https://doi.org/10.1371/journal.pone.0320849.g004

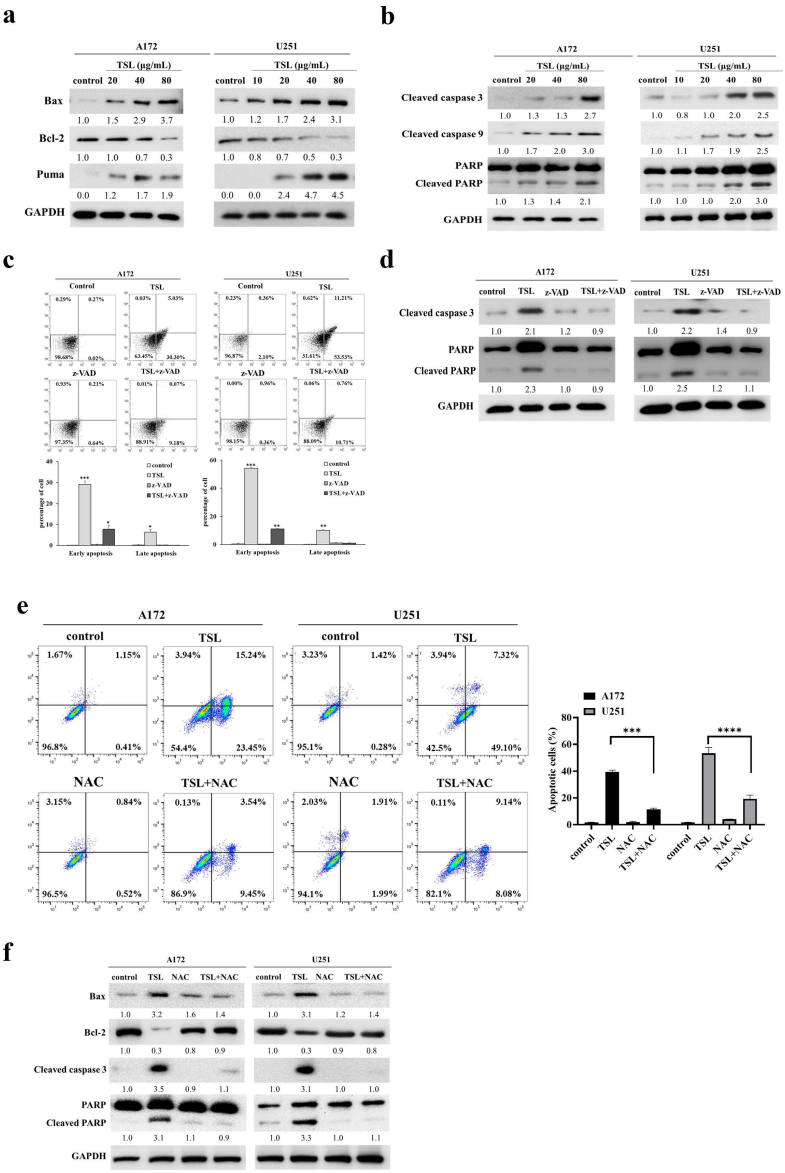

Fig 5. TSL induces apoptotic cell death via the intrinsic mitochondrial and caspase-dependent pathway. (A) Effect of TSL on the expression of PUMA, Bax and Bcl-2 proteins in GBM cell line. (B) Representative images of cleaved caspase 9, cleaved caspase 3, and PARP/cleaved PARP western blots. (C) The pan-caspase inhibitor z-VAD-FMK blocks caspase-dependent apoptosis induced by TSL in GBM. A172 and U251 cell lines were pretreated with or without the pan-caspase inhibitor z-VAD-FMK (20 μM) for 1 h and then incubated with TSL (80 ug/mL) for 48 h. Then, apoptosis was measured using flow cytometry by Annexin V-FITC and PI staining. (D) Representative images of cleaved caspase 3, and PARP/cleaved PARP western blots. (E) The antioxidant NAC blocks caspase-dependent apoptosis induced by TSL in GBM. A172 and U251 cell lines were pretreated with or without NAC (10 mM) for 30 min and then incubated with TSL (80 μg/mL) for 48 h. (F) Representative images of Western blots showing the expression levels of Bax, Bcl-2, cleaved caspase-3, and PARP/cleaved PARP. All results are shown as mean ± s.d. from three independent experiments; ***$p < 0.001$, **$p < 0.01$, *$p < 0.05$ compared with the indicated control.

https://doi.org/10.1371/journal.pone.0320849.g005

Additionally, these activators modulated the levels of proteins that were upregulated or downregulated by TSL, suggesting that activated ERK directly or indirectly regulates apoptosis-related proteins (Figs 6F and H). Taken together, our findings demonstrate that the anti-GBM activity of TSL is primarily driven by the suppression of the MEK/ERK signaling pathway.

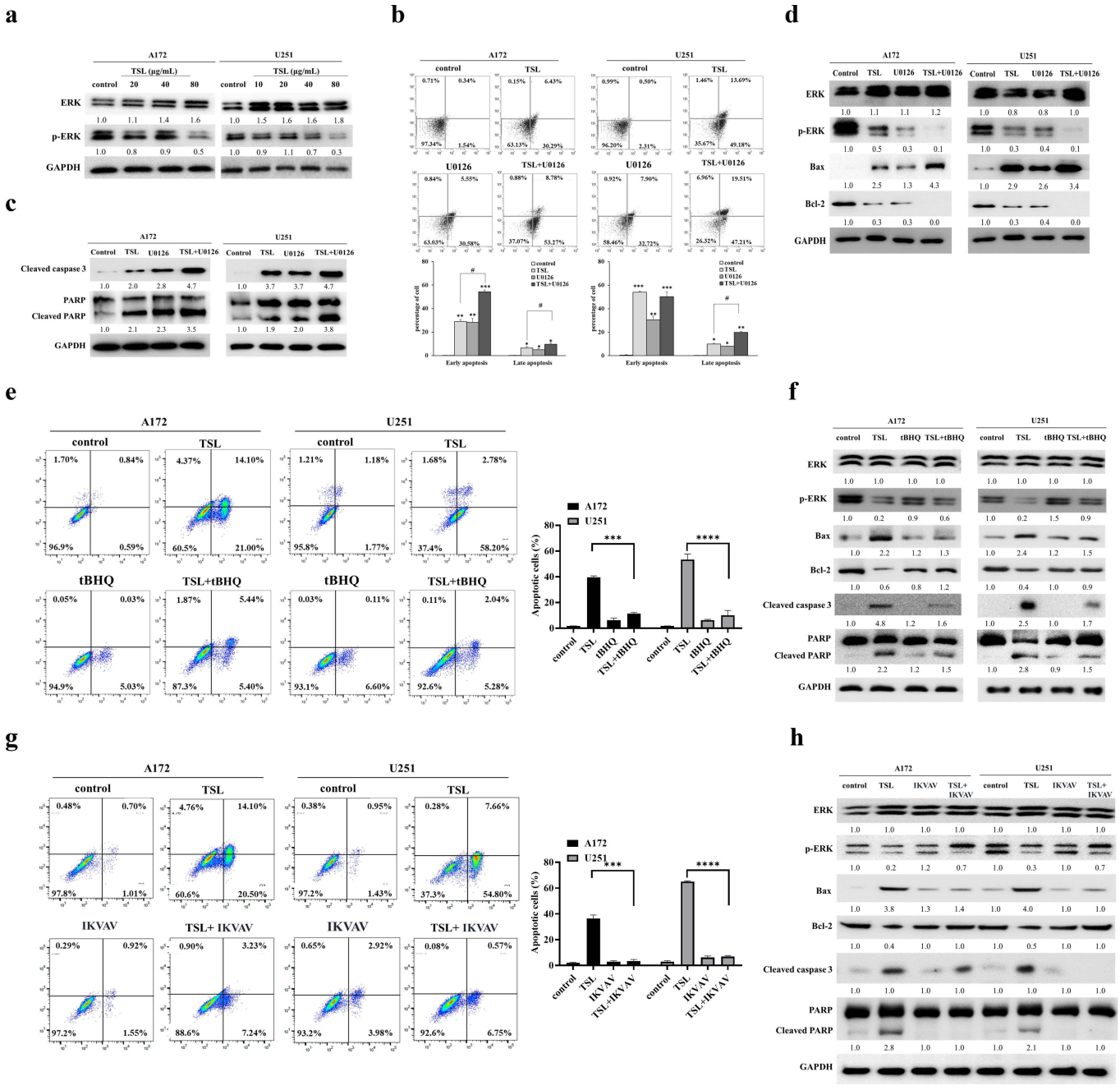

Fig 6. ERK activation is required for apoptosis induction by TSL treatment. (A) A172 and U251 cells were incubated with different concentrations of TSL for 48 h, cells were harvested and detected for ERK1/2 and p-ERK1/2 by western blot analysis. (B) The effects of MEK/ERK inhibition by U0126 on the cell death. A172 and U251 cells were treated with TSL (80 ug/mL) in the absence or presence of U0126 (10 μM) for 48 h. The proportion of apoptotic cells was detected with Annexin V-FITC and propidium iodide staining. (C) Representative images of cleaved caspase 3, and PARP/cleaved PARP western blots. (D) Representative images of ERK1/2, p-ERK1/2, Bax and Bcl-2 western blots. (E, G) The effect of ERK activation by tBHQ or IKVAV on cell death. A172 and U251 cells were treated with TSL (80 μg/mL) in the absence or presence of tBHQ (50 μM) or IKVAV (0.5 mM) for 48 h. (F, H) Representative images of ERK1/2, p-ERK1/2, Bax, Bcl-2, cleaved caspase 3, and PARP/cleaved PARP western blots. All results are shown as mean ± s.d. from three independent experiments; ***$p < 0.001$, **$p < 0.01$, *$p < 0.05$ compared with the indicated control.

https://doi.org/10.1371/journal.pone.0320849.g006

Effect of inhibiting MEK/ERK signaling pathway inhibitors on mitochondrial function subjected to TSL in GBM cells

To further elucidate the role of MEK inhibitors in mitochondrial function and apoptosis induction under TSL treatment, we measured normalized ATP levels, mitochondrial ROS, cytosolic ROS, and ΔΨm levels in the presence of TSL and the MEK inhibitor U0126. The results showed that ATP production was attenuated in the TSL and U0126 co-treatment group (Fig 7A). Conversely, mitochondrial ROS and cytosolic ROS levels were enhanced, and ΔΨm levels were decreased under TSL and U0126 treatment (Figs 7B-D). Additionally, co-treatment with IKVAV or tBHQ significantly inhibited TSL-induced cytosolic ROS in A172 and U251 cells (Fig 7E). These findings suggest that the inhibition of the MEK/ERK signaling pathway plays a key role in inducing apoptosis through ROS-mediated mitochondrial dysfunction in GBM cells treated with TSL.

TSL inhibits tumor growth in vivo

The anti-tumor efficacy of TSL was evaluated using a xenograft transplant model in NOD/SCID mice. The treatment procedure is outlined in Fig 8A. Representative tumor images (Fig 8B) clearly show a substantial reduction in tumor size in the TSL-treated group compared to the vehicle-treated group, and quantitative analysis of tumor weights (Figs 8C and D) further confirmed that TSL treatment significantly reduced tumor burden. To assess systemic effects, plasma levels of liver function markers—glutamate pyruvate transaminase (GPT) and glutamate oxaloacetate transaminase (GOT)—were measured (Fig 8E); no significant differences were observed between the two groups, indicating that TSL treatment did not induce hepatotoxicity. Additionally, no significant change in body weight was observed (Fig 8F), suggesting that TSL treatment caused minimal side effects. In parallel, the linear mixed-effects model (LME) revealed a significant effect of treatment on tumor growth over time. At baseline (Time 0), tumors in the TSL-treated group were significantly larger than those in the vehicle-treated group (Estimate = 12.53, $p = 0.0143$). Over time, tumor size increased significantly in the vehicle-treated group (Estimate = 0.75, $p < 0.0001$), whereas the TSL-treated group exhibited a markedly reduced growth rate, as evidenced by the significant Treatment × Time interaction (Estimate = -0.71, $p < 0.0001$). ANOVA confirmed significant main effects of Treatment ($p = 0.0143$), Time ($p < 0.0001$), and their interaction ($p < 0.0001$), demonstrating that the treatment altered tumor progression dynamics. Furthermore, post-hoc analysis at Time 45 showed that tumors in the TSL-treated group were significantly smaller than those in the vehicle-treated group (Estimate = 19.37, $p = 4.29 \times 10^{-5}$) (Table 1). These integrated findings indicate that although tumors in the TSL-treated group started larger, TSL treatment effectively slowed tumor growth over time, supporting its potential as an anti-tumor therapy without causing systemic toxicity.

Discussion

This study provides evidence that gallic acid is the primary bioactive component in TSL aqueous extracts and can effectively cross the BBB. Treatment with TSL demonstrated significant cytotoxic effects on U251 and A172 GBM cell lines by inducing G2/M phase cell cycle arrest and apoptosis. These effects are likely mediated through the suppression of phosphorylated MEK/ERK1/2, leading to the inhibition of ETC complexes and excessive ROS production. This cascade results in mitochondrial dysfunction, including elevated ROS levels, reduced ΔΨm, decreased ATP production, and impaired OXPHOS complexes. A model summarizing these findings is presented (Fig 9). Optimizing drug delivery systems and treatment duration will be crucial to maximizing therapeutic efficacy while minimizing potential side effects [35]. Elucidation of the anti-tumor mechanisms on the TSL will provide the opportunity to optimize adjuvant therapy for glioblastoma.

The role of gallic acid in modulating cellular signaling pathways highlights its potential in cancer treatment. Recent advances, such as adsorbing gallic acid onto gold nanoparticles (GA-GNPs), have improved its delivery and stability. GA-GNPs exhibit excellent biocompatibility, sustained release capabilities, and effective targeting of the brain tumors. These systems not only directly inhibit glioblastoma cell growth but also enhance resistance to radiation therapy,

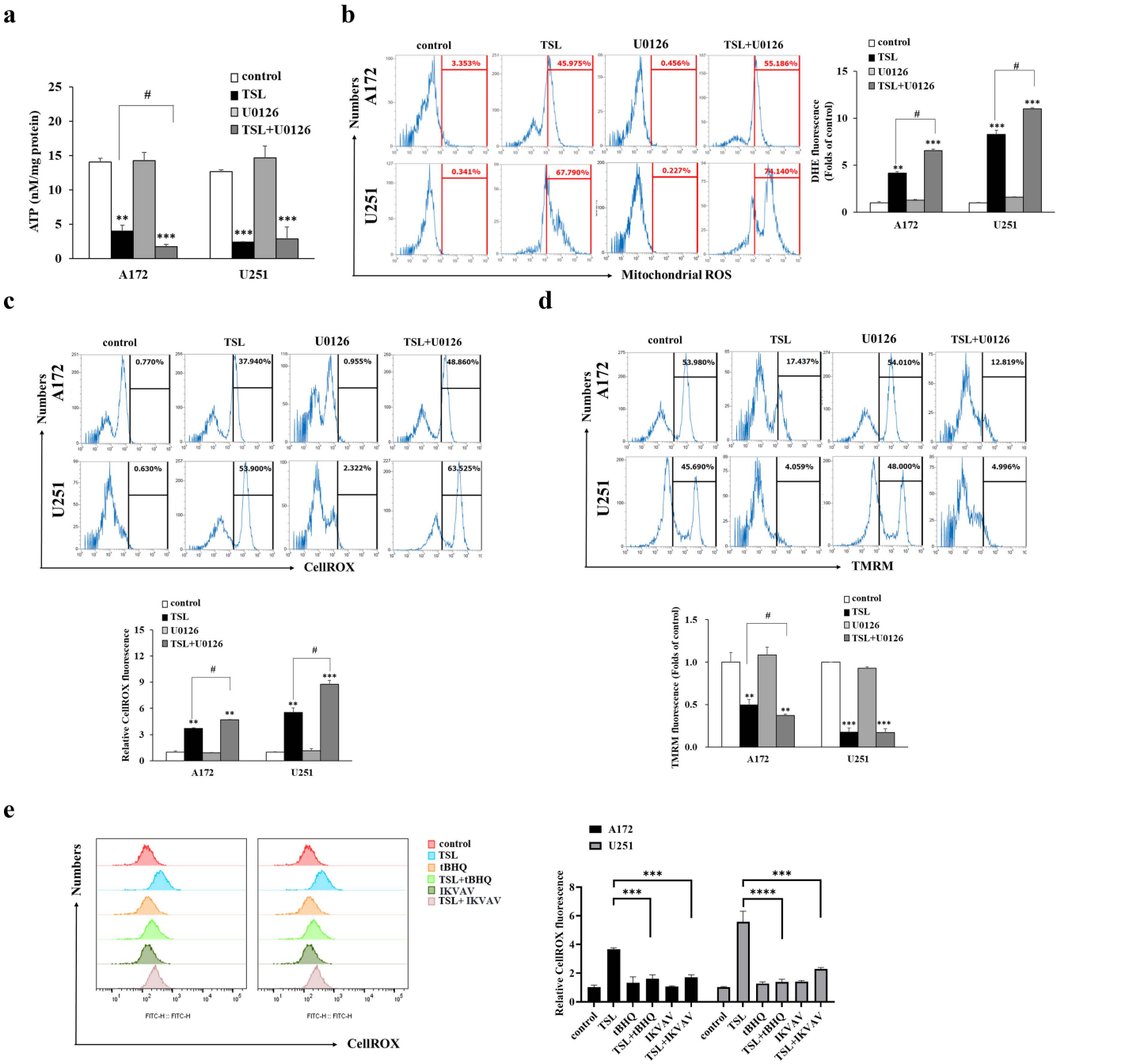

Fig 7. Effect of MAPK inhibitors on mitochondrial function in A172 and U251 cells subjected to TSL. (A) A172 and U251 cells were incubated with different concentrations of TSL for 48 h, cells were harvested and detected for normalized ATP measurements and immunoblotting analysis of OXPHOS mitochondrial complexes. (B) mitochondrial ROS, (C) cytosolic ROS and (D) ΔΨm levels were measured using flow cytometry and fluorescence microscopy with DHE Deep Red, CellROX Deep green, and TMRM Deep Red staining, respectively, and indicated by representative histograms are shown in parallel with bar graphs showing the relative TMRM mean relative fluorescence intensity. (E) The effects of activator of ERK by tBHQ or IKVAV on the cytosolic ROS. All results are shown as mean ± s.d. from three independent experiments; ***$p < 0.001$, **$p < 0.01$, *$p < 0.05$ compared with the indicated control.

https://doi.org/10.1371/journal.pone.0320849.g007

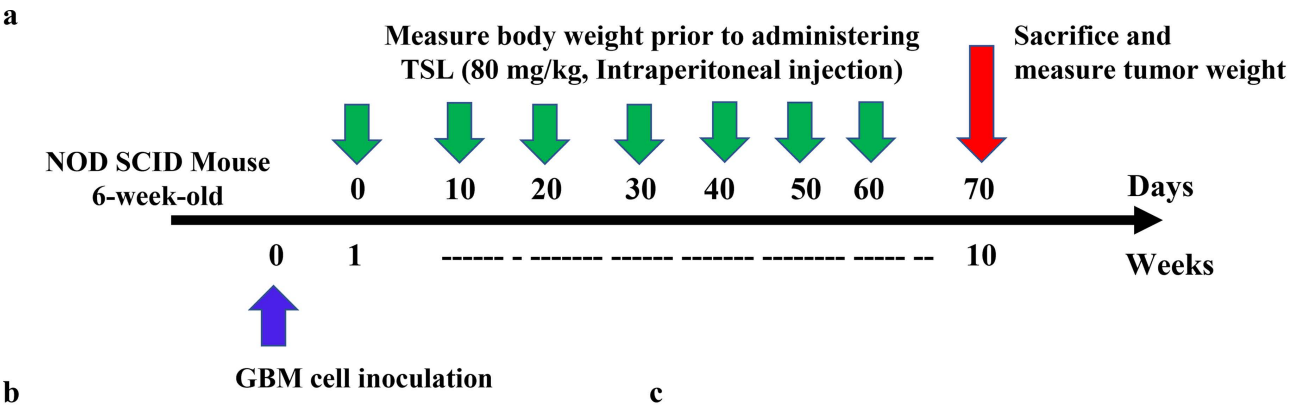

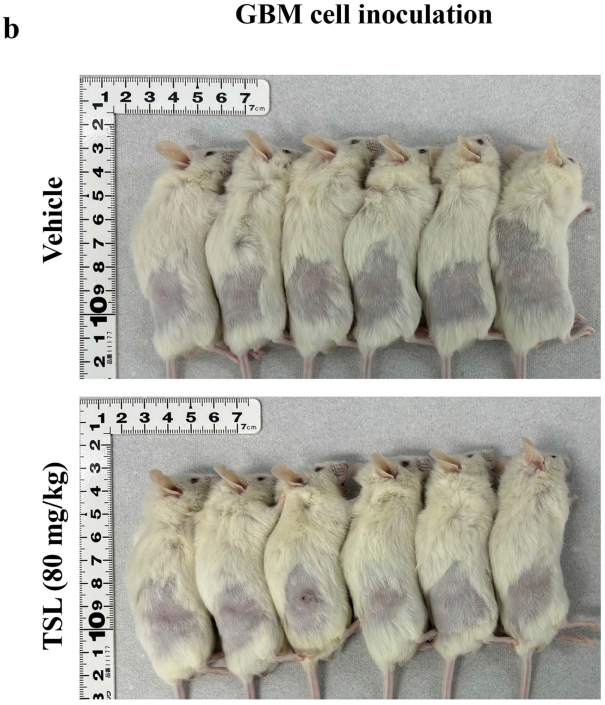

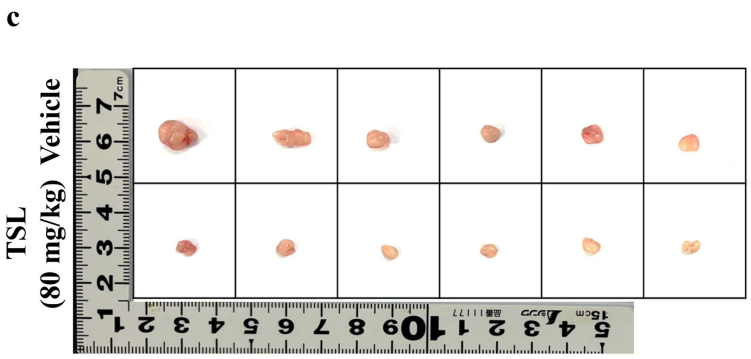

e

	Vehicle	TSL 80 mg/kg
GOT	115.1± 28.9	114.9± 12.5
GPT	44.26± 9.4	45.2± 4.21

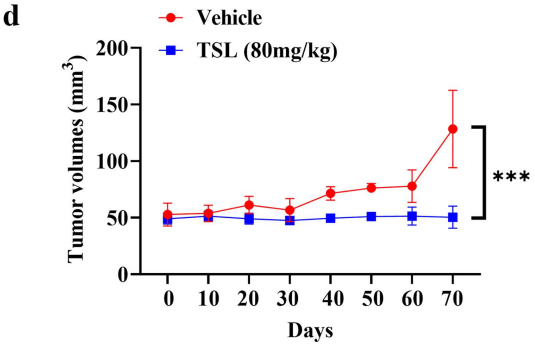

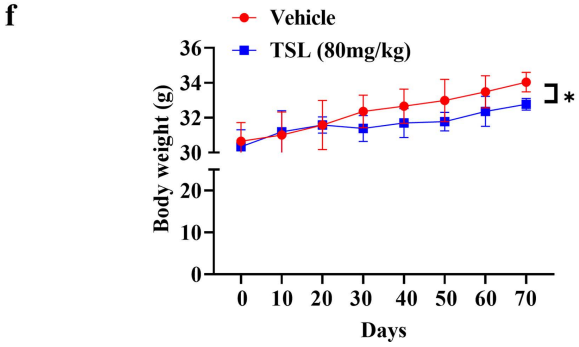

Fig 8. TSL Suppresses Tumor Formation in GBM Cells Using a Xenograft Mouse Model. (A) Schematic representation of the TSL treatment schedule in 6-week-old NOD/SCID mice. GBM cells were injected subcutaneously, and tumor formation was allowed for one week (week 0). From week 1 to week 10, mice were administered TSL (80 mg/kg) intraperitoneally three times per week, while the vehicle group received DMSO. Body weight was monitored weekly before each TSL injection. Tumors were harvested and measured at week 10. (B) Representative images of tumors from the

vehicle-treated (top row) and TSL-treated (bottom row) groups at week 10 (n = 6). A ruler is included for size reference. (C, D) Quantification of tumor weights in vehicle and TSL-treated groups at week 10. (E) Plasma levels of GPT and GOT in both groups after 10 weeks of treatment. (F) Body weight progression from day 1 to day 70 in untreated and treated groups. Error bars represent ± SD. Statistical analysis was performed using a t-test, with ***p < 0.001, **p < 0.01, *p < 0.05 indicating significance.

https://doi.org/10.1371/journal.pone.0320849.g008

Table 1. Summary of statistical analyses for tumor volume differences over time.

Effect	Time point[a]		Estimate	SE	F.value	t.value	p.value
LME Model Results							
(Intercept)	NA		37.67	3.52	NA	10.71	8.13×10^{-16}
Treatment	NA		12.53	4.97	NA	2.52	1.43×10^{-2}
Time	NA		0.75	0.064	NA	11.61	5.43×10^{-19}
Treatment x Time	NA		-0.71	0.091	NA	-7.78	1.89×10^{-11}
ANOVA Results							
Treatment	NA		NA	NA	6.35	NA	1.43×10^{-2}
Time	NA		NA	NA	74.58	NA	3.82×10^{-13}
Treatment x Time	NA		NA	NA	60.55	NA	1.89×10^{-11}
Post-Hoc Comparisons							
Vehicle-Treatment	45	19.37	2.81	NA		6.88	4.29×10^{-5}

a.represents the number of days the animals have been in the study.

https://doi.org/10.1371/journal.pone.0320849.t001

improving overall treatment efficacy [36]. Future studies integrating gallic acid with GNP-based delivery systems could further optimize drug targeting and prolong therapeutic effects, paving the way for new approaches in treating neural tumors.

We investigated the molecular mechanisms underlying TSL-induced apoptosis in GBM cells. Figs 2 and 3 demonstrate that TSL functions as both a proliferation inhibitor and an apoptosis inducer in a dose- and time-dependent manner. Morphological analysis reveals white and refringent clusters of cells, indicative of detaching and dying cells [37]. These findings are consistent with reports that TSL activates a preexisting apoptotic pathway [27,38]. Specifically, TSL activates PARP, caspase-9, and caspase-3 prior to apoptosis onset, increases the expression of pro-apoptotic Bax and Puma, and decreases the expression of anti-apoptotic Bcl-xL. Changes in the Bax/Bcl-xL ratio contribute to the pro-apoptotic effects of TSL. Additionally, TSL inhibits cancer cell proliferation by arresting cells in the G2/M phase (Fig 2A).

Mitochondria are central to TSL-induced apoptosis, primarily through intrinsic mitochondrial dysfunction and caspase-dependent pathways. A critical event in this process is mitochondrial outer membrane permeabilization (MOMP), which is regulated by the balance between pro-apoptotic proteins such as Bax and Puma, and anti-apoptotic proteins like Bcl-2 and Bcl-xL [39,40]. TSL treatment in GBM cells shifts this balance by upregulating Bax and Puma while downregulating Bcl-2 and Bcl-xL, thereby promoting mitochondrial-mediated apoptosis. This leads to mitochondrial permeability transition, dissipation of $\Delta\Psi m$, and reduced ATP production, indicating early mitochondrial dysfunction (Figs 4 and 5) [41].

The activation of cleaved caspase-9, caspase-3, and PARP confirms the involvement of a caspase-dependent pathway. Although PARP cleavage is typically associated with extrinsic apoptotic pathways, the data suggest its role in apoptosis driven by mitochondrial dysfunction. Notably, TSL-induced mitochondrial disruption occurs early in the apoptotic process, even though $\Delta\Psi m$ loss is traditionally considered a late apoptotic event (Fig 4) [42]. Together, these findings demonstrate that TSL-induced apoptosis is mediated by intrinsic mitochondrial dysfunction, characterized by early $\Delta\Psi m$ dissipation, impaired ATP generation, and subsequent caspase activation (Figs 4 and 5).

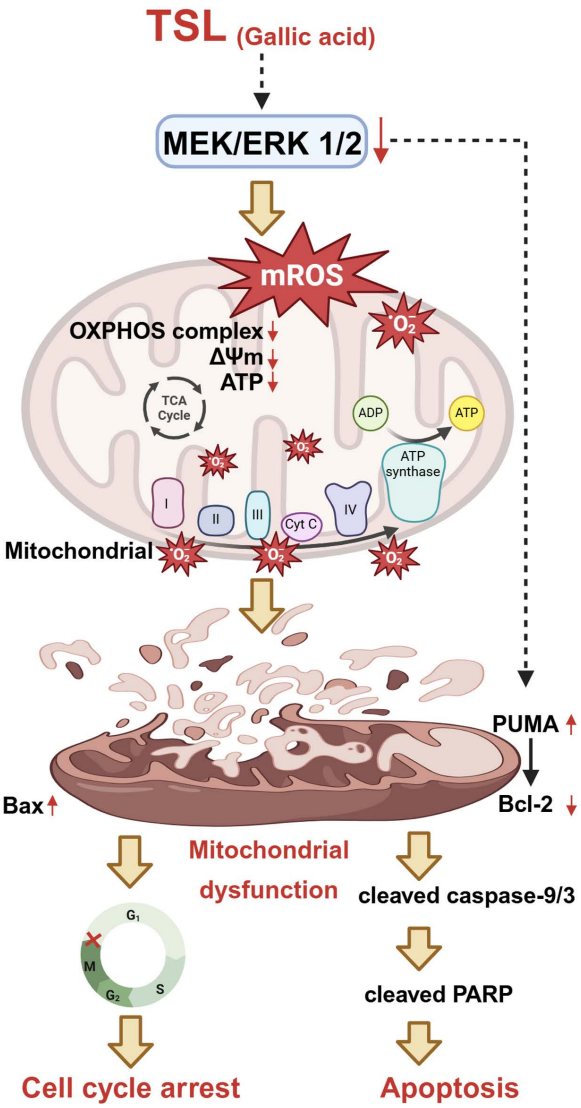

Fig 9. Model for TSL treatment in GBM cells. After TSL treatment, MEK/ERK pathway was inhibited which lead to mitochondria ROS degeneration, then decreased OXPHOS complexes that attenuated ATP production, and caused mitochondria dysfunction eventually. Upregulation of pro-apoptotic proteins (Bax and Puma) and downregulation of anti-proapoptotic protein (Bcl-2) were also illustrated and leaded to mitochondria dysfunction. Finally, caspase-dependent apoptosis (cleaved caspase-3, 9 and PARP) was induced in the last event under TSL treatment in GBM cells.

https://doi.org/10.1371/journal.pone.0320849.g009

Mitochondria are a major ROS source during apoptosis [43]. Reduced ΔΨm increases ROS generation, further inducing apoptosis and reducing ATP production. This also leads to increased mitochondria ROS and cytosolic ROS levels. Enhanced ROS production has been linked to chemotherapy-induced apoptosis [44,45], and in this study, we hypothesize that intracellular ROS production is a critical factor for the apoptosis induced by the treatment. The treatment increased mitochondrial and cytosolic ROS levels (Figs 4C and D). To validate this hypothesis, cells treated with the antioxidant NAC prior to the treatment showed a reversal of apoptosis, supporting the role of intracellular ROS production as a key factor in inducing apoptosis (Figs 5E and F). The ROS production induced by the treatment appears cumulative, occurring in multiple steps.

The MEK/ERK signaling pathway plays a crucial role in cell survival and proliferation, and its dysregulation is associated with cancer progression. Suppression of ERK and phosphorylated ERK (p-ERK) levels was observed, leading to mitochondrial dysfunction through increased ROS production [46,47]. The treatment reduced p-ERK levels (Fig 6A), suggesting that inhibiting ERK phosphorylation plays a role in inducing apoptosis via ROS-mediated mitochondrial dysfunction. Using the MEK/ERK inhibitor U0126 together with the treatment further enhanced ERK suppression, leading to increased apoptosis, as evidenced by elevated levels of pro-apoptotic proteins (Bax and Puma), caspase-3 activation, and reduced ΔΨm and ATP production (Figs 6 and 7). Conversely, the ERK activators tBHQ and IKVAV peptide reversed these effects, decreasing apoptosis markers and ROS levels (Figs 6E-H and 7E). Although the non-specific antioxidant effects of tBHQ and the dual ERK/AKT activation by IKVAV peptide complicate interpretations, further studies are required to clarify the precise role of ERK signaling in these responses [48,49].

In a xenograft model, treatment effectively suppressed tumor growth without affecting body weight. However, variations in tumor growth dynamics were observed across experimental setups. Subcutaneous injection of 1×10^6 U87 MG cells into nude mice typically results in tumors reaching ~100 mm^3 by Day 11 [50], whereas in our study, no tumor growth was observed at this time point. Similarly, 2×10^6 T98G cells injected into nude mice required 46 days to form tumors of ~500 mm^3 [51]. SCID mice are generally superior for xenograft studies due to their enhanced tumor growth and metastasis potential compared to nude mice. Quantitative analyses indicate that SCID mice, particularly under whole-body irradiation, require significantly lower tumor cell doses for successful transplantation [52]. Despite using 6×10^6 T98G cells for subcutaneous injection into NOD/SCID mice, no tumor formation was observed within 46 days in our study. Slow tumor growth has also been reported in other studies, where T98G cells (4.3×10^6) injected into nude mice formed tumors only after Day 70 [53]. These findings align with our observations and highlight the variability in tumor formation timelines. Subcutaneous xenograft models, while simple and reproducible, fail to replicate the invasive and infiltrative microenvironment of human GBM. This often leads to tumor necrosis, destabilizing experimental outcomes and limiting their utility for studying metastasis and invasion mechanisms crucial to glioblastoma progression. Additionally, delayed cell injection post-preparation can further reduce tumor formation success [54]. The small tumor volumes observed in this study (<150 mm^3) also introduce significant measurement variability, especially with the limited number of animals per experimental condition, impacting statistical robustness. Although standard practices for subcutaneous models typically involve initiating measurements when tumors reach 200–250 mm^3, variability in tumor growth rates, as observed in our study and others (Fig 8) [51,53], made it challenging to adhere to these practices due to delayed tumor formation.

These findings highlight the potential of gallic acid to induce cytotoxic effects in GBM cells through ROS-mediated mitochondrial dysfunction and inhibition of the MEK/ERK signaling pathway. This research establishes TSL as a promising therapeutic candidate for glioblastoma, warranting further clinical investigation. To enhance the translational relevance, future studies should prioritize orthotopic implantation models over subcutaneous models, as they better replicate the clinical characteristics of glioblastoma.

Acknowledgments

We thank Wallace Academic Editing for English edition on the manuscript. The presentation of the manuscript as a preprint. Preprint according to the following link: https://www.researchsquare.com/article/rs-1837153/v1. The authors thank the center for research resources and development in kaohsiung medical university for the assistance in flow cytometry image analysis. The authors thank the center for laboratory animals in kaohsiung medical university for the animal care.

Author contributions

Conceptualization: cheng yu Tsai, Tai-Hsin Tsai.

Data curation: Hui-Yuan Su.

Formal analysis: Keng-Liang Kuo.

Funding acquisition: Keng-Liang Kuo.

Investigation: Chih-Lung Lin.

Methodology: Chieh-Hsin Wu.

Project administration: Chieh-Hsin Wu.

Resources: Joon-Khim Loh.

Supervision: Ann-Shung Lieu, Aij-Lie Kwan.

Validation: Wen-Chang Chang.

Visualization: Fu-Long Huang.

Writing – original draft: cheng yu Tsai, Yu-Feng Su.

Writing – review & editing: cheng yu Tsai, Yu-Feng Su.

References

1. Louis DN, Perry A, Reifenberger G, von Deimling A, Figarella-Branger D, Cavenee WK, et al. The 2016 World health organization classification of tumors of the central nervous system: a summary. Acta Neuropathol. 2016;131(6):803–20. https://doi.org/10.1007/s00401-016-1545-1 PMID: 27157931
2. Miller CR, Perry A. Glioblastoma. Arch Pathol Lab Med. 2007;131(3):397–406. https://doi.org/10.5858/2007-131-397-G PMID: 17516742
3. Park JK, Hodges T, Arko L, Shen M, Dello Iacono D, McNabb A, et al. Scale to predict survival after surgery for recurrent glioblastoma multiforme. J Clin Oncol. 2010;28(24):3838–43. https://doi.org/10.1200/JCO.2010.30.0582 PMID: 20644085
4. Stupp R, Mason WP, van den Bent MJ, Weller M, Fisher B, Taphoorn MJB, et al. Radiotherapy plus concomitant and adjuvant temozolomide for glioblastoma. N Engl J Med. 2005;352(10):987–96. https://doi.org/10.1056/NEJMoa043330 PMID: 15758009
5. Minniti G, Amelio D, Amichetti M, Salvati M, Muni R, Bozzao A, et al. Patterns of failure and comparison of different target volume delineations in patients with glioblastoma treated with conformal radiotherapy plus concomitant and adjuvant temozolomide. Radiother Oncol. 2010;97(3):377–81. https://doi.org/10.1016/j.radonc.2010.08.020 PMID: 20855119
6. Lee SY. Temozolomide resistance in glioblastoma multiforme. Genes Dis. 2016;3(3):198–210. https://doi.org/10.1016/j.gendis.2016.04.007 PMID: 30258889
7. Alonso MM, Gomez-Manzano C, Bekele BN, Yung WKA, Fueyo J. Adenovirus-based strategies overcome temozolomide resistance by silencing the O6-methylguanine-DNA methyltransferase promoter. Cancer Res. 2007;67(24):11499–504. https://doi.org/10.1158/0008-5472.CAN-07-5312 PMID: 18089777
8. Le Rhun E, Preusser M, Roth P, Reardon DA, van den Bent M, Wen P, et al. Molecular targeted therapy of glioblastoma. Cancer Treat Rev. 2019;80:101896. https://doi.org/10.1016/j.ctrv.2019.101896 PMID: 31541850
9. Cabrini G, Fabbri E, Lo Nigro C, Dechecchi MC, Gambari R. Regulation of expression of O6-methylguanine-DNA methyltransferase and the treatment of glioblastoma (Review). Int J Oncol. 2015;47(2):417–28. https://doi.org/10.3892/ijo.2015.3026 PMID: 26035292
10. Han S, Li Z, Master LM, Master ZW, Wu A. Exogenous IGFBP-2 promotes proliferation, invasion, and chemoresistance to temozolomide in glioma cells via the integrin β1-ERK pathway. Br J Cancer. 2014;111(7):1400–9. https://doi.org/10.1038/bjc.2014.435 PMID: 25093489
11. Annovazzi L, Mellai M, Schiffer D. Chemotherapeutic Drugs: DNA damage and repair in glioblastoma. Cancers (Basel). 2017;9(6):57. https://doi.org/10.3390/cancers9060057 PMID: 28587121
12. Trachootham D, Zhou Y, Zhang H, Demizu Y, Chen Z, Pelicano H, et al. Selective killing of oncogenically transformed cells through a ROS-mediated mechanism by beta-phenylethyl isothiocyanate. Cancer Cell. 2006;10(3):241–52. https://doi.org/10.1016/j.ccr.2006.08.009 PMID: 16959615
13. Circu ML, Aw TY. Reactive oxygen species, cellular redox systems, and apoptosis. Free Radic Biol Med. 2010;48(6):749–62. https://doi.org/10.1016/j.freeradbiomed.2009.12.022 PMID: 20045723
14. García-Ruiz C, Colell A, Marí M, Morales A, Fernández-Checa JC. Direct effect of ceramide on the mitochondrial electron transport chain leads to generation of reactive oxygen species. Role of mitochondrial glutathione. J Biol Chem. 1997;272(17):11369–77. https://doi.org/10.1074/jbc.272.17.11369 PMID: 9111045
15. Aggarwal V, Tuli HS, Varol A, Thakral F, Yerer MB, Sak K, et al. Role of reactive oxygen species in cancer progression: molecular mechanisms and recent advancements. Biomolecules. 2019;9(11):735. https://doi.org/10.3390/biom9110735 PMID: 31766246
16. Lin Y-H. MicroRNA networks modulate oxidative stress in cancer. Int J Mol Sci. 2019;20(18):4497. https://doi.org/10.3390/ijms20184497 PMID: 31514389
17. Okon IS, Zou M-H. Mitochondrial ROS and cancer drug resistance: Implications for therapy. Pharmacol Res. 2015;100:170–4. https://doi.org/10.1016/j.phrs.2015.06.013 PMID: 26276086

18. Edmonds JM, Staniforth M. Plate 348. Toona sinensis. Curtis's Botanical Magazine. 1998;15(3):186–93. https://doi.org/10.1111/1467-8748.00169
19. Sun X, Zhang L, Cao Y, Gu Q, Yang H, Tam JP. Quantitative analysis and comparison of four major flavonol glycosides in the leaves of Toona sinensis (A. Juss.) Roemer (Chinese Toon) from various origins by high-performance liquid chromatography-diode array detector and hierarchical clustering analysis. Pharmacogn Mag. 2016;12(Suppl 2):S270-6. https://doi.org/10.4103/0973-1296.182160 PMID: 27279719
20. Yang H-L, Chen S-C, Lin K-Y, Wang M-T, Chen Y-C, Huang H-C, et al. Antioxidant activities of aqueous leaf extracts of Toona sinensis on free radical-induced endothelial cell damage. J Ethnopharmacol. 2011;137(1):669–80. https://doi.org/10.1016/j.jep.2011.06.017 PMID: 21718778
21. Hseu Y-C, Chang W-H, Chen C-S, Liao J-W, Huang C-J, Lu F-J, et al. Antioxidant activities of Toona Sinensis leaves extracts using different anti-oxidant models. Food Chem Toxicol. 2008;46(1):105–14. https://doi.org/10.1016/j.fct.2007.07.003 PMID: 17703862
22. Wang P-H, Tsai M-J, Hsu C-Y, Wang C-Y, Hsu H-K, Weng C-F. Toona sinensis Roem (Meliaceae) leaf extract alleviates hyperglycemia via altering adipose glucose transporter 4. Food Chem Toxicol. 2008;46(7):2554–60. https://doi.org/10.1016/j.fct.2008.04.011 PMID: 18495317
23. Liao J-W, Hsu C-K, Wang M-F, Hsu W-M, Chan Y-C. Beneficial effect of Toona sinensis Roemor on improving cognitive performance and brain degeneration in senescence-accelerated mice. Br J Nutr. 2006;96(2):400–7. https://doi.org/10.1079/bjn20061823 PMID: 16923237
24. Hsiang C-Y, Hseu Y-C, Chang Y-C, Kumar KJS, Ho T-Y, Yang H-L. Toona sinensis and its major bioactive compound gallic acid inhibit LPS-induced inflammation in nuclear factor-κB transgenic mice as evaluated by in vivo bioluminescence imaging. Food Chem. 2013;136(2):426–34. https://doi.org/10.1016/j.foodchem.2012.08.009 PMID: 23122080
25. Chen C-J, Michaelis M, Hsu H-K, Tsai C-C, Yang KD, Wu Y-C, et al. Toona sinensis Roem tender leaf extract inhibits SARS coronavirus replication. J Ethnopharmacol. 2008;120(1):108–11. https://doi.org/10.1016/j.jep.2008.07.048 PMID: 18762235
26. Chia Y-C, Rajbanshi R, Calhoun C, Chiu RH. Anti-neoplastic effects of gallic acid, a major component of Toona sinensis leaf extract, on oral squamous carcinoma cells. Molecules. 2010;15(11):8377–89. https://doi.org/10.3390/molecules15118377 PMID: 21081858
27. Chen H-M, Wu Y-C, Chia Y-C, Chang F-R, Hsu H-K, Hsieh Y-C, et al. Gallic acid, a major component of Toona sinensis leaf extracts, contains a ROS-mediated anti-cancer activity in human prostate cancer cells. Cancer Lett. 2009;286(2):161–71. https://doi.org/10.1016/j.canlet.2009.05.040 PMID: 19589639
28. Wang C-Y, Lin K-H, Yang C-J, Tsai J-R, Hung J-Y, Wang P-H, et al. Toona sinensis extracts induced cell cycle arrest and apoptosis in the human lung large cell carcinoma. Kaohsiung J Med Sci. 2010;26(2):68–75. https://doi.org/10.1016/s1607-551x(10)70010-3 PMID: 20123594
29. Yang H-L, Kuo Y-T, Vudhya Gowrisankar Y, Lin K-Y, Hsu L-S, Huang P-J, et al. The leaf extracts of toona sinensis and fermented culture broths of antrodia camphorata synergistically cause apoptotic cell death in promyelocytic leukemia cells. Integr Cancer Ther. 2020;19:1534735420923734. https://doi.org/10.1177/1534735420923734 PMID: 32618215
30. Chen Y-C, Chien L-H, Huang B-M, Chia Y-C, Chiu H-F. Aqueous Extracts of Toona sinensis Leaves Inhibit Renal Carcinoma Cell Growth and Migration Through JAK2/stat3, Akt, MEK/ERK, and mTOR/HIF-2α Pathways. Nutr Cancer. 2016;68(4):654–66. https://doi.org/10.1080/01635581.2016.1158292 PMID: 27115866
31. Su Y, Yang Y-C, Hsu H-K, Hwang S-L, Lee K-S, Lieu A-S, et al. Toona sinensis leaf extract has antinociceptive effect comparable with non-steroidal anti-inflammatory agents in mouse writhing test. BMC Complement Altern Med. 2015;15:70. https://doi.org/10.1186/s12906-015-0599-2 PMID: 25886358
32. Tsai C-Y, Ko H-J, Chiou S-J, Lai Y-L, Hou C-C, Javaria T, et al. NBM-BMX, an HDAC8 inhibitor, overcomes temozolomide resistance in glioblastoma multiforme by downregulating the β-Catenin/c-Myc/SOX2 pathway and upregulating p53-Mediated MGMT inhibition. Int J Mol Sci. 2021;22(11):5907. https://doi.org/10.3390/ijms22115907 PMID: 34072831
33. Ko H-J, Tsai C-Y, Chiou S-J, Lai Y-L, Wang C-H, Cheng J-T, et al. The phosphorylation status of Drp1-Ser637 by PKA in mitochondrial fission modulates Mitophagy via PINK1/Parkin to exert multipolar spindles assembly during mitosis. Biomolecules. 2021;11(3):424. https://doi.org/10.3390/biom11030424 PMID: 33805672
34. Tsai C-Y, Ko H-J, Huang C-YF, Lin C-Y, Chiou S-J, Su Y-F, et al. Ionizing Radiation Induces Resistant Glioblastoma Stem-Like Cells by Promoting Autophagy via the Wnt/β-Catenin Pathway. Life (Basel). 2021;11(5):451. https://doi.org/10.3390/life11050451 PMID: 34069945
35. Pathak N, Singh P, Singh PK, Sharma S, Singh RP, Gupta A, et al. Biopolymeric nanoparticles based effective delivery of bioactive compounds toward the sustainable development of anticancerous therapeutics. Front Nutr. 2022;9:963413. https://doi.org/10.3389/fnut.2022.963413 PMID: 35911098
36. Jing Z, Li M, Wang H, Yang Z, Zhou S, Ma J, et al. Gallic acid-gold nanoparticles enhance radiation-induced cell death of human glioma U251 cells. IUBMB Life. 2021;73(2):398–407. https://doi.org/10.1002/iub.2436 PMID: 33372372
37. Bury M, Punzo B, Berestetskiy A, Lallemand B, Dubois J, Lefranc F, et al. Evaluation of the anticancer activities of two fungal polycyclic ethanones, alternethanoxins A and B, and two of their derivatives. Int J Oncol. 2011;38(1):227–32. PMID: 21109944
38. Chen H-M, Wu Y-C, Chia Y-C, Chang F-R, Hsu H-K, Hsieh Y-C, et al. Gallic acid, a major component of Toona sinensis leaf extracts, contains a ROS-mediated anti-cancer activity in human prostate cancer cells. Cancer Lett. 2009;286(2):161–71. https://doi.org/10.1016/j.canlet.2009.05.040 PMID: 19589639
39. Kale J, Osterlund EJ, Andrews DW. BCL-2 family proteins: changing partners in the dance towards death. Cell Death Differ. 2018;25(1):65–80. https://doi.org/10.1038/cdd.2017.186 PMID: 29149100
40. Soldani C, Lazzè MC, Bottone MG, Tognon G, Biggiogera M, Pellicciari CE, et al. Poly(ADP-ribose) polymerase cleavage during apoptosis: when and where?. Exp Cell Res. 2001;269(2):193–201. https://doi.org/10.1006/excr.2001.5293 PMID: 11570811

41. Hussar P. Apoptosis Regulators Bcl-2 and Caspase-3. Encyclopedia. 2022;2(4):1624–36. https://doi.org/10.3390/encyclopedia2040111
42. Ly JD, Grubb DR, Lawen A. The mitochondrial membrane potential (deltapsi(m)) in apoptosis; an update. Apoptosis. 2003;8(2):115–28. https://doi.org/10.1023/a:1022945107762 PMID: 12766472
43. Deragon MA, McCaig WD, Patel PS, Haluska RJ, Hodges AL, Sosunov SA, et al. Mitochondrial ROS prime the hyperglycemic shift from apoptosis to necroptosis. Cell Death Discov. 2020;6(1):132. https://doi.org/10.1038/s41420-020-00370-3 PMID: 33298902
44. Gao Z-Y, Liu Z, Bi M-H, Zhang J-J, Han Z-Q, Han X, et al. Metformin induces apoptosis via a mitochondria-mediated pathway in human breast cancer cells in vitro. Exp Ther Med. 2016;11(5):1700–6. https://doi.org/10.3892/etm.2016.3143 PMID: 27168791
45. Zorov DB, Juhaszova M, Sollott SJ. Mitochondrial reactive oxygen species (ROS) and ROS-induced ROS release. Physiol Rev. 2014;94(3):909–50. https://doi.org/10.1152/physrev.00026.2013 PMID: 24987008
46. Burotto M, Chiou VL, Lee J-M, Kohn EC. The MAPK pathway across different malignancies: a new perspective. Cancer. 2014;120(22):3446–56. https://doi.org/10.1002/cncr.28864 PMID: 24948110
47. Sugiura R, Satoh R, Takasaki T. ERK: a double-edged sword in cancer. ERK-dependent apoptosis as a potential therapeutic strategy for cancer. Cells. 2021;10(10):2509. https://doi.org/10.3390/cells10102509 PMID: 34685488
48. Yang B, Huang H, He Q, Lu W, Zheng L, Cui L. Tert-Butylhydroquinone prevents oxidative stress-mediated apoptosis and extracellular matrix degradation in rat chondrocytes. Evid Based Complement Alternat Med. 2021;2021:1905995. https://doi.org/10.1155/2021/1905995 PMID: 34925524
49. Li B, Qiu T, Zhang P, Wang X, Yin Y, Li S. IKVAV regulates ERK1/2 and Akt signalling pathways in BMMSC population growth and proliferation. Cell Prolif. 2014;47(2):133–45. https://doi.org/10.1111/cpr.12094 PMID: 24617901
50. Ovcharenko D, Chitjian C, Kashkin A, Fanelli A, Ovcharenko V. Two dichloric compounds inhibit in vivo U87 xenograft tumor growth. Cancer Biol Ther. 2019;20(9):1281–9. https://doi.org/10.1080/15384047.2019.1632131 PMID: 31234707
51. Wang X-Q, Bai H-M, Li S-T, Sun H, Min L-Z, Tao B-B, et al. Knockdown of HDAC1 expression suppresses invasion and induces apoptosis in glioma cells. Oncotarget. 2017;8(29):48027–40. https://doi.org/10.18632/oncotarget.18227 PMID: 28624794
52. Taghian A, Budach W, Zietman A, Freeman J, Gioioso D, Ruka W, et al. Quantitative comparison between the transplantability of human and murine tumors into the subcutaneous tissue of NCr/Sed-nu/nu nude and severe combined immunodeficient mice. Cancer Res. 1993;53(20):5012–7. PMID: 8402692
53. Honma K, Miyata T, Ochiya T. Type I collagen gene suppresses tumor growth and invasion of malignant human glioma cells. Cancer Cell Int. 2007;7:12. https://doi.org/10.1186/1475-2867-7-12 PMID: 17578585
54. Palanichamy K, Acus K, Jacob J, Chakravarti A. Clinically relevant brain tumor model and device development for experimental therapeutics. J Anal Oncol. 2015;4(1). https://doi.org/10.6000/1927-7229.2015.04.01.2